

## **Chapter 7**

# **Optical devices based on porous silicon multilayers**

In this chapter we present multilayer optical devices fabricated with porous silicon. All these devices have been designed using the realized simulation programs and the mathematical study presented in chapters 3 and 4. They have been fabricated with the fabrication system explained and calibrated in chapter 5 and their optical response, specially the reflectivity spectrum, has been studied.

The optical devices presented here are DBRs, microcavities and omnidirectional mirrors. The optical response of a microcavity has been studied under different humidity conditions. The application of the periodic structure is evaluated for obtaining omnidirectional mirrors. Finally, the omnidirectional bandgap of a new structure consisting of periodic structures stacked together is studied.

## 7.1. Distributed Bragg Reflector

### 7.1.1. Fabrication and characterization

The DBR consists of the periodic repetition of two layers obtained with different current densities, and therefore with different refractive indices. The two current densities chosen for the fabrication of this DBR are 30 and 70 mA/cm<sup>2</sup>. For its formation we have used p<sup>+</sup>-type silicon wafers with a resistivity of 0.01 Ω·cm and ethanoic HF electrolyte with concentration of 15.4% (volumetric ratio).

The calibration of the fabrication system, realized with the measurement of interference fringes method (MIF) and SEM, indicated that for J=70 mA/cm<sup>2</sup>, the refractive index varies from 1.33 to 1.28 for the wavelength range between 1 and 4 μm and the etch rate is 49.7 nm/s. For J=30 mA/cm<sup>2</sup>, the etch rate is 26.7 nm/s and its refractive index varies between 1.72 and 1.65 for the same wavelength range. This multilayer has been obtained with the lateral-wafer cell, therefore the calibration of the system is different than the one presented in section 5.3, that was the calibration for the system with the bottom-wafer cell.

These refractive indices obtained with these current densities are very low, probably due to the low HF concentration used for the electrolyte, only 15.4 % (vol). These refractive indices agree with the ones obtained by other authors for similar HF concentrations [103]. For higher concentrations of HF, higher values of refractive index are possible for the same current densities [39,102].

The DBR was fabricated by applying the current densities J=30 mA/cm<sup>2</sup> (obtaining the n<sub>H</sub> layer) and 70 mA/cm<sup>2</sup> (for the n<sub>L</sub> layer) for 10 s. According to the etch rate calculated from the characterization of the monolayers, the thickness of the layers are supposed to be approximately h<sub>H</sub>=267 nm and h<sub>L</sub>=500 nm, respectively. The period thickness is expressed as  $\Lambda = h_H + h_L$ . Fig. 7.1 shows the cross section of the fabricated multilayer. The dark gray layers correspond to the layers with n<sub>L</sub> and the light gray are the ones with refractive index n<sub>H</sub>. The number of periods of the measured multilayer is 15.

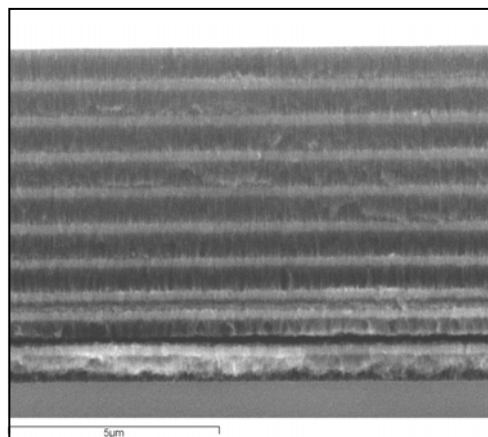


Fig. 7.1. SEM image of the fabricated multilayer. The light gray layers are the high refractive index ones that are thinner than and the low refractive index layers (dark gray layers).

The characterization of the DBR has been realized studying its reflectivity spectrum with the FTIR spectrometer Bruker Vertex 70 within the wavelength range from 1 to 4  $\mu\text{m}$ . Fig. 7.2 shows the FTIR reflectivity spectrum measurements of the fabricated multilayer for different angles of incidence: 12, 30, 44, 50, 58 and 66 degrees. We can observe that the multilayer presents a high reflectivity band that is centered approximately at 2.2  $\mu\text{m}$  for incidence angle 12°. When the angle of incidence increases, the high reflectivity band not only shifts to lower wavelengths, but also becomes narrower and its maximum decreases. For angles of incidence higher than 50° the maximum reflectivity is lower than 1.

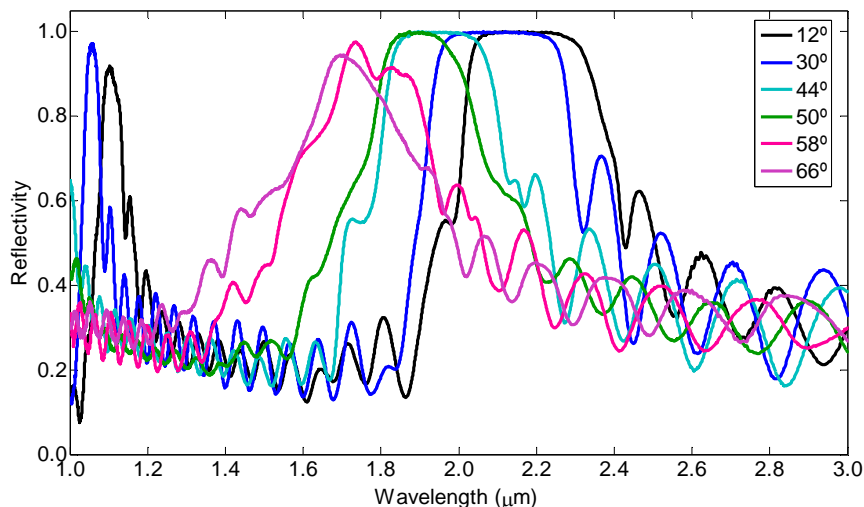


Fig. 7.2. Reflectivity spectra of the fabricated DBR, measured for six different angles of incidence. The bandgap can be clearly observed centered approximately at  $\lambda=2.2 \mu\text{m}$  for  $\theta=12^\circ$  and shifts to the left when the incidence angle increases.

### 7.1.2. Simulation

The fabricated multilayer structure has been simulated using the programs realized for this purpose. As has been explained in section 5.2.2, the variation of the refractive index in the studied wavelength range is small (less than 5%), for this reason, the refractive indices used for the simulation have been considered constant and with approximate values  $n_L=1.3$  and  $n_H=1.7$ . The thicknesses of the layers have been adjusted by fitting the simulation to the experimental spectra and are  $h_L=500 \text{ nm}$  and  $h_H=270 \text{ nm}$ , which are in good agreement with the calculated etching rate. The simulated and the measured reflectivity spectra of the multilayer are presented for three different angles of incidence in Fig. 7.3. The agreement between the measured and the simulated spectra shows that the parameters of the fabricated DBR (refractive indices and thicknesses) are approximately the ones expected from the formation parameters (current density and etch time), which demonstrates the control of

the etching process. Besides, this fact shows that the behavior of the DBR can be theoretically described.

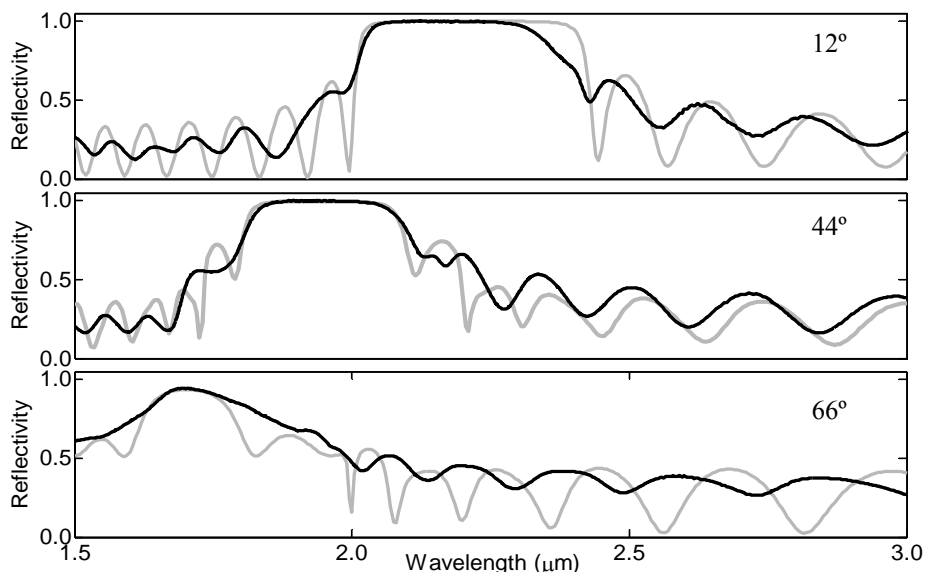


Fig. 7.3. Reflectivity spectra of the fabricated DBR for angles of incidence 12°, 44° and 66°. The thick solid lines represent measured spectra, whereas the gray solid lines are the simulated spectra.

For a particular wavelength  $\lambda$ , it is possible to calculate from the projected band structure (PBS) [116] the range of incidence angles for which the reflectivity is near 1. Fig. 7.4 shows the PBS of the fabricated multilayer. For a given wavelength  $\lambda$  (corresponding to  $\omega\Lambda/2\pi c$ ),  $\beta\Lambda/2\pi$  is related to the angle of incidence  $\theta_i$  with  $\beta=(\omega/c)n_i\sin(\theta_i)$ . The light line indicates the relation between  $\omega\Lambda/2\pi c$  and  $\beta\Lambda/2\pi$  for incidence angle 90° in air. The shaded region represents the allowed states and the white region within the light lines represents the bandgap, that corresponds to the high reflectivity band. Although in the PBS both polarizations are represented, TM polarization is more restrictive than TE, therefore the TM polarization bandgap limits will be observed.

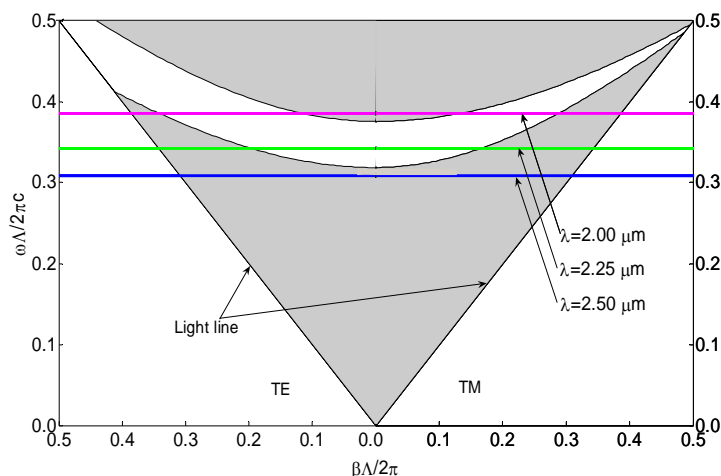


Fig. 7.4. Projected band structure (PBS) of the studied multilayer. The lines indicate the normalized frequencies corresponding to  $\lambda=2, 2.25$  and  $2.5 \mu\text{m}$ .

We now analyze the particular cases of three different  $\lambda$ :  $2.50, 2.25$  and  $2.00 \mu\text{m}$ . For  $\lambda=2.5 \mu\text{m}$  ( $\omega\Lambda/2\pi c=0.308$ ) there is no bandgap for any angle of incidence  $\theta_i$  (Fig. 7.4). This can be also observed in Fig. 7.2, where the reflectivity for this wavelength is low for any  $\theta_i$ . For  $\lambda=2.25 \mu\text{m}$  ( $\omega\Lambda/2\pi c=0.342$ ), the bandgap exists for  $\theta_i=0^\circ$  to  $\theta_i=30^\circ$ . This fact is shown in Fig. 7.2, where we can see that for  $12^\circ$  and  $30^\circ$  the reflectivity at  $\lambda=2.25 \mu\text{m}$  is near 1 but for higher angles it is very low. Finally, for  $2 \mu\text{m}$  ( $\omega\Lambda/2\pi c=0.385$ ) the bandgap only exists for  $\theta_i$  from  $20^\circ$  to  $48^\circ$ . In Fig. 7.3 this fact is clearly visible. We can observe that for  $12^\circ$  the reflectivity at  $\lambda=2 \mu\text{m}$  is low (this angle does not belong to the bandgap), when  $\theta_i=44^\circ$  the reflectivity is 1 (bandgap) and when  $\theta_i$  increases ( $66^\circ$ ) the reflectivity is low again because this angle does not belong to the bandgap. Hence, it is demonstrated that for any wavelength, the range of incidence angles for which the bandgap exists can be studied with the projected band structure.

## 7.2. Microcavity

### 7.2.1. Fabrication, characterization and simulation

The porous silicon microcavity has been obtained by the electrochemical etching of p+-type silicon wafers with a resistivity of  $0.01\Omega\cdot\text{cm}$  in an ethanoic HF electrolyte with concentration of 15.4% (volumetric ratio). Fig. 7.5 shows the schematic of the microcavity and the SEM image of the fabricated microcavity, that consists of a spacer layer inserted in between two symmetric Distributed Bragg Reflectors (DBR). Each DBR has three periods. Each period consists of two layers with different refractive indices ( $n_1$ ,  $n_2$ ) and thicknesses ( $d_1$ ,  $d_2$ ).

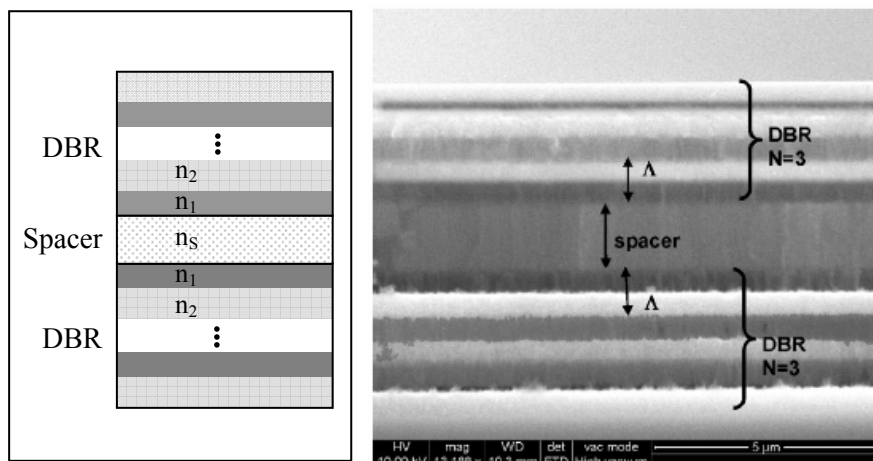


Fig. 7.5. Left: Schematic of the microcavity structure. Right: SEM image of the fabricated porous silicon microcavity. The spacer layer is located in between two DBR. Each DBR is formed by the periodic repetition ( $N=3$ ) of two layers with low refractive index (gray layer) and high refractive index (light gray layer).

These values of refractive indices and thicknesses have been used to simulate the optical properties of the porous silicon microcavity using the transfer matrix method. Fig. 7.6 shows the simulated reflectivity spectrum assuming an incidence angle of  $20^\circ$ , where we can observe the reflectivity resonance around  $3 \mu\text{m}$ . Fig. 7.6 also shows the experimental reflectivity spectrum of the microcavity for an incidence angle  $20^\circ$  using a FTIR spectrometer Bruker Vertex 70. The spectrum is characterized by a reflectivity resonance at  $2.97 \mu\text{m}$  in between two high reflectivity bands, in good agreement with the simulated results. Narrower resonance widths could be obtained either by increasing the number of periods of the DBR or by enhancing the fabrication conditions [98].

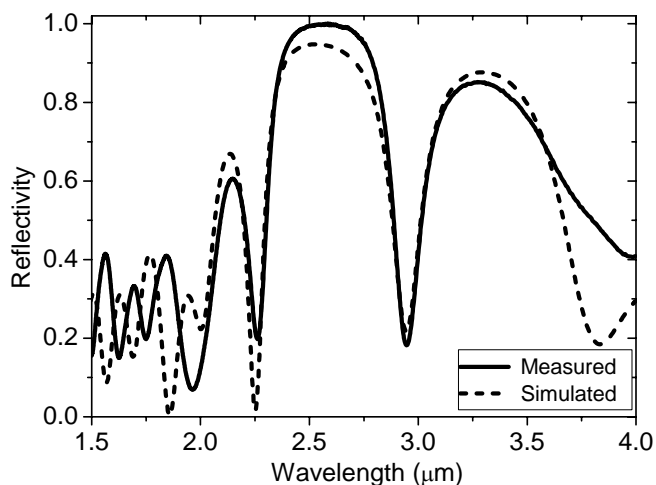


Fig. 7.6. Measured (solid line) and simulated (dashed line) reflectivity spectrum of the fabricated microcavity for incidence angle  $20^\circ$ . The reflectivity resonance is situated at  $\lambda=2.97 \mu\text{m}$ . The differences between the measured and the simulated spectra are due to the anisotropy of the low refractive index layers that is not considered in the simulation program.



## 7.2.2. Influence of the relative humidity on the reflectivity spectrum of the microcavity

Fig. 7.7 shows the measured reflectivity spectrum of the fabricated microcavity for different humidity levels. The changes in the spectrum are small, in good agreement with previous results [135]. The inset in Fig. 7.7 shows the zoom of reflectivity resonance and its fitting by using a Gaussian function. We can observe that when humidity increases, the reflectivity resonance shifts to higher wavelengths and its reflectivity decreases. Fig. 7.8a shows this resonance shift. The reflectivity spectrum of the microcavity is recovered when the humidity returns to the initial laboratory conditions.

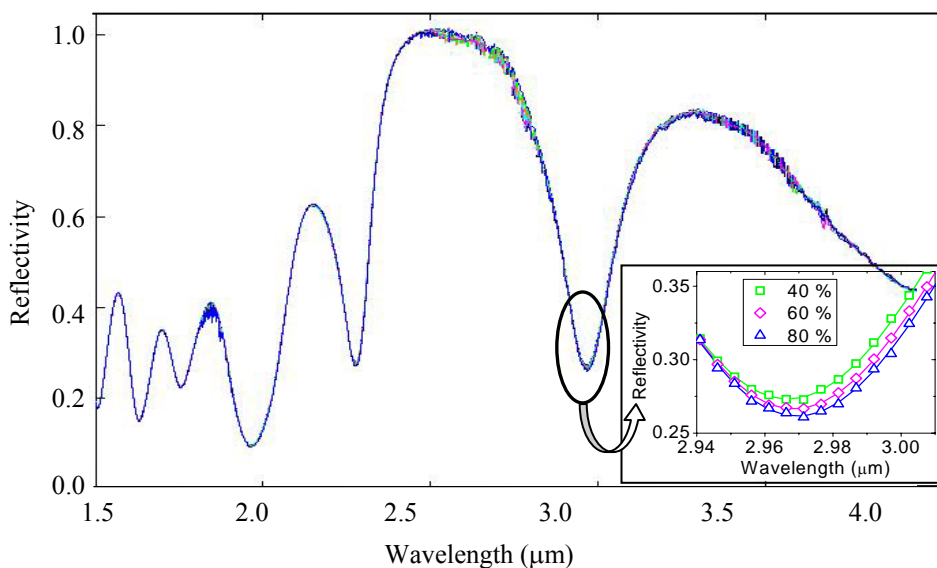


Fig. 7.7. Measured reflectivity spectrum for humidity levels of 40%, 50%, 60%, 70% and 80%. Inset: Zoom of the measured (symbol) reflectivity spectrum of the microcavity centered at the reflectivity resonance for humidity levels of 40%, 60% and 80%. The solid lines are the fitted values using a Gaussian function.

These variations are probably due to water vapor infiltrated into the pores of the porous silicon layers. Water vapor slightly increases the effective refractive index of the layers as the air in the pores is substituted by water vapor. As the increase of the refractive index is very slight, we can explain the slight shift of the reflectivity resonance to higher wavelengths and the decrease of the reflectivity when the humidity rises.

To quantify the sensor sensitivity at a given  $\lambda$ , we define the merit function R as

$$R = \frac{R_H - R_{H_{\max}}}{R_{H_{\max}}} \times 100(\%) \quad (7.1)$$

where  $R_{H_{\max}}$  is the measured reflectivity for the maximum relative humidity and  $R_H$  is the measured reflectivity for a given relative humidity. Fig. 7.8b shows the linear dependence of this merit function for  $\lambda = 3 \mu\text{m}$  in the humidity range from 35% to 80%, where  $R_{H_{\max}}$  is 0.324 for 80%.

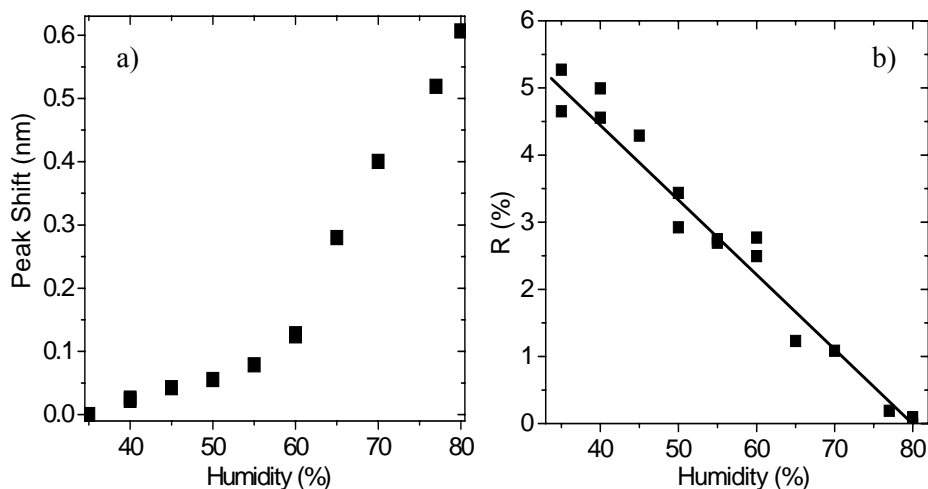


Fig. 7.8. a) Variation of the reflectivity resonance position for different humidity levels b) Variation of the merit function, defined by the Eq. (7.1), for different humidity levels at  $\lambda = 3 \mu\text{m}$ . The linear dependence is also shown.

### 7.2.3. Water condensation on the surface of the microcavity

In this section, we study the changes in the reflectivity spectrum when water is not only present as vapor infiltrated into the pores but also as a thin film on the surface of the microcavity due to the water condensation.

Fig. 7.9 shows the measured reflectivity spectrum of the microcavity for different humidity levels with condensed water on the surface. The initial reflectivity measurement was realized when the microcavity was in a 60% relative humidity with a condensed water film on its surface. This measurement presents very low reflectivity values for the whole wavelength range. After this measurement, a desiccant has been inserted into the FTIR sample compartment to reduce the humidity of the ambient and the condensation on the microcavity, and the rest of measurements have been realized at different times during this drying process. We observe that when the humidity decreases, the reflectivity increases for the whole range of wavelengths and the position of the reflectivity resonance is also affected.

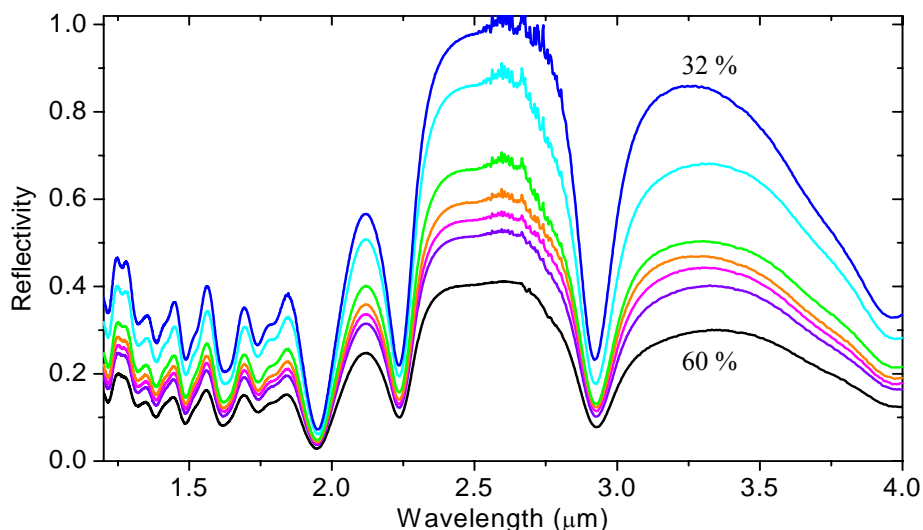


Fig. 7.9. Measured reflectivity spectrum for different humidity levels with the presence of condensed water on the surface of the microcavity. The lowest humidity level measured in 32 % and the highest is 60 %.

To quantify the relative reflectivity variation, we used the merit function defined by the Eq. (7.1). Fig. 7.10a shows the merit function  $R$  for  $\lambda=3 \mu\text{m}$ , where  $R_{\text{Hmax}}$  is 0.167 for 60%. The obtained values follow an exponential law instead of the linear law obtained in the previous section. According to these results, we could say that the condensation on the surface could mask the humidity measurements of this type of sensor. Fig. 7.10b shows the resonance shift. We can observe that the thin film of condensed water on the microcavity surface leads to larger shifts than when there is only water vapor infiltrated into the pores.

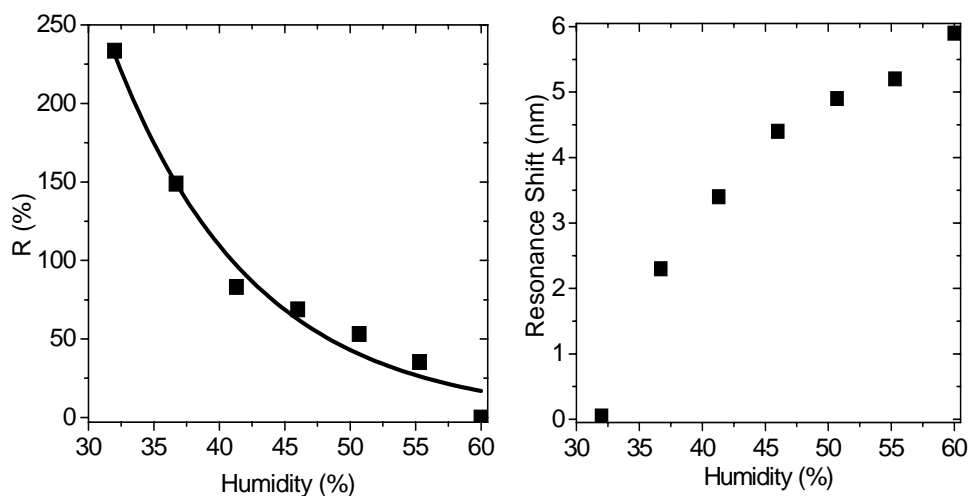


Fig. 7.10 a) Variation of the merit function for different humidity levels at  $\lambda=3 \mu\text{m}$ . The exponential dependence is also shown, b) Variation of the reflectivity resonance position for different humidity levels.

## 7.3. Omnidirectional mirrors

Omnidirectional mirrors are characterized by their omnidirectional bandgap, that is the wavelength range where the reflectivity is the unity for any incidence angle and any polarization. All the parameters that determine the existence and the width of the omnidirectional bandgap have been already discussed in detail in chapter 4. In this section, we present some multilayer structures fabricated with porous silicon and we study the existence of an omnidirectional bandgap for all of them. Firstly, the widely used periodic structure is evaluated. Secondly, a new structure consisting of several periodic structures stacked together is fabricated and characterized and its suitability for obtaining omnidirectional mirrors is studied.

### 7.3.1. Design, fabrication and characterization of periodic structures

The periodic omnidirectional mirror structure consists of the periodic repetition of two layers obtained with different current densities. In chapter 4, a detailed study of the parameters that influence on the optical behavior of this structure has been presented.

For the fabrication of this periodic mirror we have chosen the current densities  $J_1=10 \text{ mA/cm}^2$  and  $J_2=50 \text{ mA/cm}^2$ . Current densities lower than  $10 \text{ mA/cm}^2$  yielded porous layers with very slow etch rates, increasing the duration of the layer formation without a significant gain in the index. Current densities higher than  $50 \text{ mA/cm}^2$  yielded fragile porous layers that could not be characterized using spectroscopic ellipsometry.

For the fabrication of this structure,  $p^+$ -type silicon wafers with a resistivity of  $0.01 \text{ } \Omega\cdot\text{cm}$  and ethanoic HF electrolyte with concentration of 15.4% (volumetric ratio) have been used. For these formation parameters, the fabrication system of porous silicon layers has been calibrated (section 4.3). According to this calibration, for  $J_1=10 \text{ mA/cm}^2$ , the refractive index varies from 2.21 to 2.12 for the wavelength range between 1 and  $4 \text{ } \mu\text{m}$  and the etch rate is approximately  $10.7 \text{ nm/s}$ . For  $J_2=50 \text{ mA/cm}^2$ , the etch rate is estimated to

be 36 nm/s and its refractive index varies between 1.5 and 1.45 for the same wavelength range.

From the theoretical study, we know that to obtain a mirror with the omnidirectional bandgap centered at  $\lambda=1.55 \mu\text{m}$ , the bandgap for normal incidence has to be centered at approximately  $\lambda=1.6 \mu\text{m}$ . The thickness of the layers for each refractive index determines this center wavelength. The layer thicknesses that lead to this center wavelength are approximately  $d_1=171.2 \text{ nm}$ , and  $d_2=288 \text{ nm}$ , being the period thickness  $\Lambda=d_1+d_2=459.2 \text{ nm}$ .

The reflectivity spectrum of this periodic multilayer has been simulated using one of the developed programs. For the simulation, the refractive index of each layer has been supposed to be constant because its variation in the studied wavelength range is very small (less than 5%). The refractive indices used for the simulation are  $n_1=2.15$  and  $n_2=1.45$  and the thicknesses are the ones calculated:  $d_1=171.2 \text{ nm}$ , and  $d_2=288 \text{ nm}$ . The number of periods is 15. Fig. 7.11 shows the simulated reflectivity spectrum of this periodic structure for normal incidence. We can observe that the bandgap is centered at  $\lambda=1.6 \mu\text{m}$ .

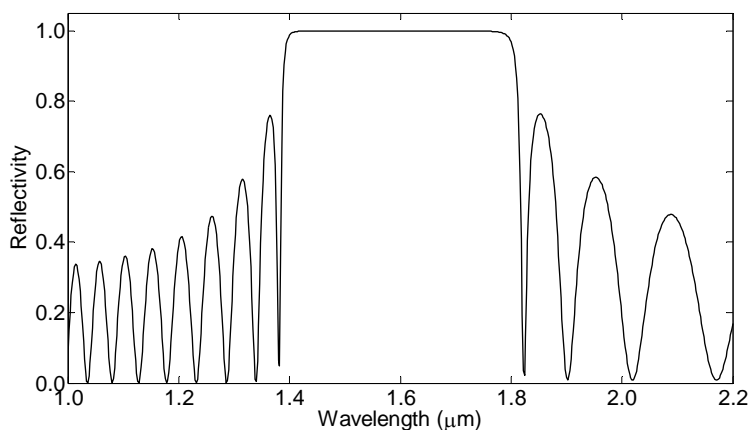


Fig. 7.11. Simulated reflectivity spectrum of the periodic structure for normal incidence. The bandgap is centered approximately at  $\lambda=1.6 \mu\text{m}$ .

This designed structure has been fabricated. The refractive indices of the layers are determined by the current densities and the thicknesses are determined by the etching times. From the etch rate we calculate the etching times needed to obtain the desired thicknesses. For the current densities used, the etching times that lead to these thicknesses are  $t_1=16$  s for  $J_1$ , and  $t_2=8$  s for  $J_2$ . The number of periods is 15. The reflectivity spectrum of the fabricated multilayer has been measured with the FTIR spectrometer Bruker Vertex 70 within the wavelength range from 1 to 3  $\mu\text{m}$ . Fig. 7.12 shows the measured reflectivity spectra for different incidence angles. The lowest incidence angle that can be measured with this FTIR is  $12^\circ$  and we can observe that for this incidence angle the bandgap is centered approximately at  $\lambda=1.58$   $\mu\text{m}$ . When the incidence angle increases the bandgap width decreases and shifts to lower wavelengths. The highest incidence angle that can be measured with the FTIR is approximately  $65^\circ$  because reflectivity spectra measured for incidence angles between  $65^\circ$  and  $80^\circ$  are partially affected by the sample holder.

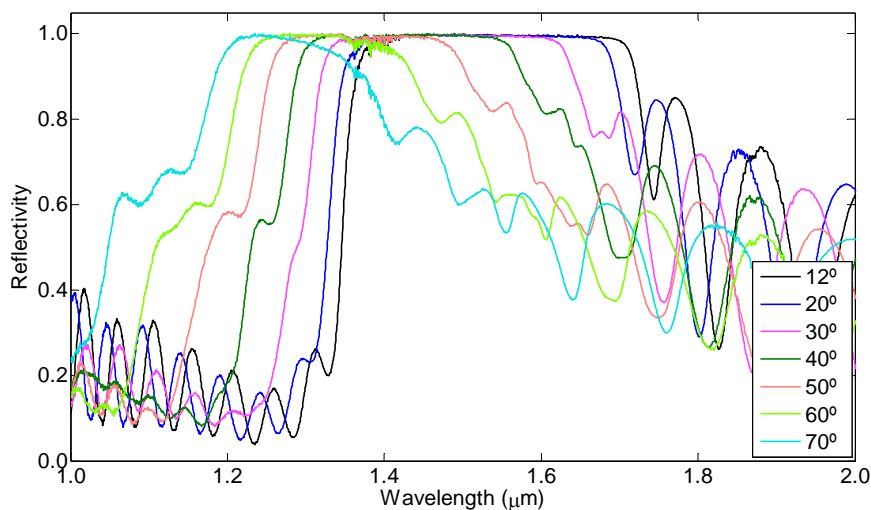


Fig. 7.12. Measured reflectivity spectrum of the periodic structure for seven different incidence angles. The bandgap is centered approximately at  $1.58$   $\mu\text{m}$  for incidence angle  $12^\circ$ . When the incidence angle increases the bandgap shifts to lower wavelengths.

From this figure, we can observe that the periodic multilayer structure has not an omnidirectional bandgap. It has a bandgap for an interval of incidence angles that goes from  $\theta=12^\circ$  to approximately  $\theta=60^\circ$ . It is not an omnidirectional mirror. This agrees with the theoretical study, where we deduced that to obtain an omnidirectional mirror, the high refractive index of the periodic multilayer must be higher than 2.25. The refractive index range obtainable with our fabrication conditions goes from 1.45 to 2.15 therefore to obtain an omnidirectional mirror one of the new structures proposed in chapter 4 consisting on different periodic structures stacked together has been designed and fabricated.

### 7.3.2. Design of a new omnidirectional mirror structure

We now study the reflectivity spectrum of a multilayer consisting of two different periodic structures (PS) stacked together. The schematic structure of this multilayer can be observed in Fig. 7.13.

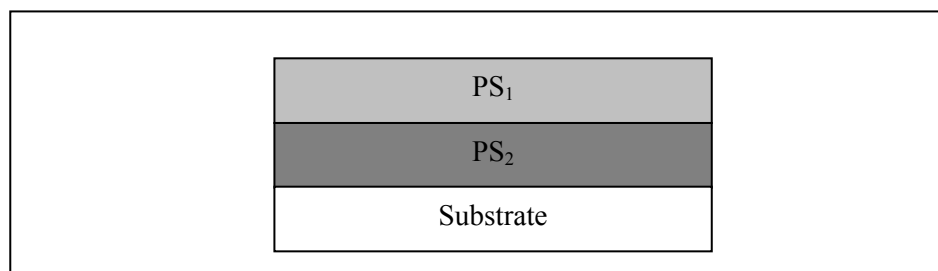


Fig. 7.13. Schematic of the multilayer formed by two periodic structures stacked together.

The theoretical study demonstrated that the bandgap of a multilayer formed by two structures stacked together is the union of the bandgaps of the two structures (section 3.3.1.4). This stacked structure presents a wider bandgap



for all the incidence angles and therefore an omnidirectional bandgap could be obtained.

The two periodic structures that form this multilayer have to be appropriately chosen for the widening of the bandgap. The first periodic structure ( $PS_1$ ) is the one described in the previous section. The second one ( $PS_2$ ) is designed to have a bandgap centered at a slightly higher wavelength than the bandgap of  $PS_1$ . The refractive indices of  $PS_2$  are the same used for  $PS_1$ :  $n_1=2.15$  and  $n_2=1.45$ . Due to the small bandgap shift desired and to ease the fabrication process, we have chosen a larger thickness for the high refractive index layer whereas the thickness for the low refractive index layer remains the same. The chosen thicknesses for the layers of  $PS_2$  are  $d_1=214$  nm, and  $d_2=288$  nm, being the period thickness  $\Lambda=d_1+d_2=502$   $\mu\text{m}$ .

Fig. 7.14 shows the simulated reflectivity spectrum of  $PS_2$  for normal incidence and it is compared with the one of  $PS_1$ . The number of periods of both PS is 15. We can observe that both spectra intersect.

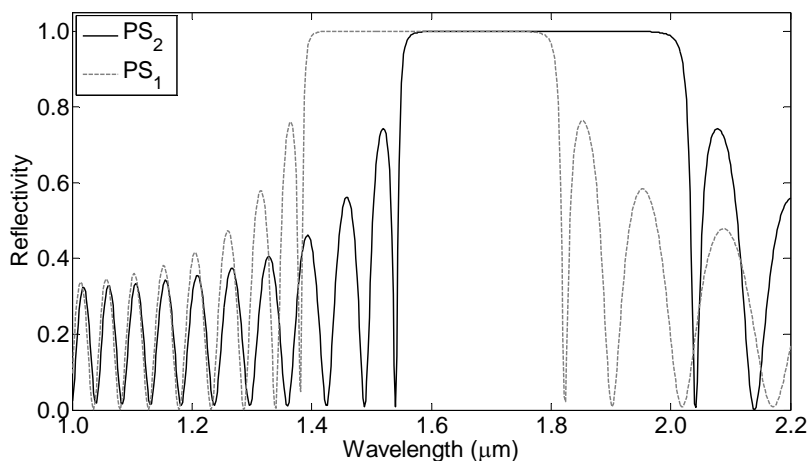


Fig. 7.14. Simulated reflectivity spectrum of  $PS_2$  (black line). It can be compared with the reflectivity spectrum of  $PS_1$  (dashed gray line). Both spectra have been simulated for normal incidence.

The simulated reflectivity spectrum of the stacked structure is represented in Fig. 7.15. The refractive indices used for the simulation are  $n_1=2.15$  and  $n_2=1.45$ . The thicknesses are the ones calculated before for each PS. The incidence angles simulated are the ones that determine the existence of the omnidirectional bandgap. The simulated spectra show that this structure has an omnidirectional bandgap, therefore it is an omnidirectional mirror. With this result it is demonstrated that the limitations of the refractive index range can be overcome by the use of this new stacked structure proposed.

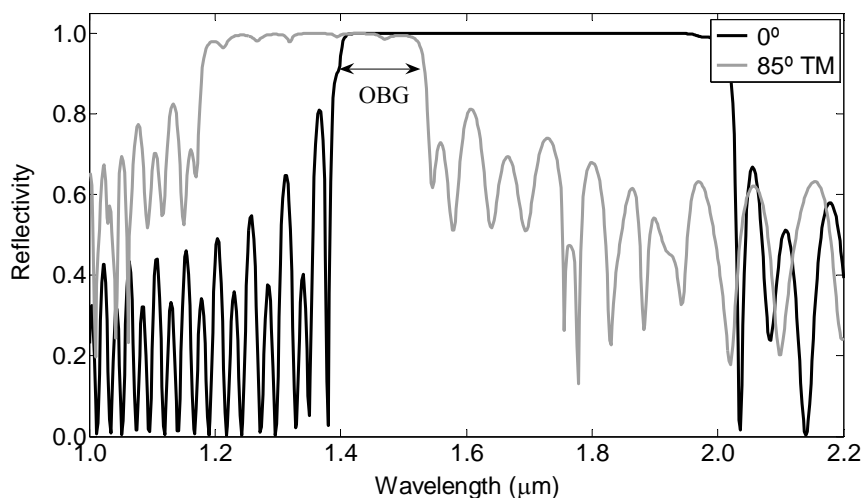


Fig. 7.15. Simulated reflectivity spectra of the stacked structure for incidence angles  $\theta=0^\circ$  and  $\theta=85^\circ$ . The omnidirectional bandgap (OBG) is indicated.

### 7.3.3. Fabrication and characterization of the new omnidirectional mirror structure

The stacked multilayer consisting of the two PS stacked together has been fabricated using  $p^+$ -type silicon wafers with a resistivity of  $0.01 \Omega\cdot\text{cm}$  and ethanoic HF electrolyte with concentration of 15.4% (volumetric ratio). The current densities applied are  $J_1=10 \text{ mA/cm}^2$  and  $J_2=50 \text{ mA/cm}^2$ . For 15 periods the etching times are  $t_1=16 \text{ s}$  for  $J_1$ , and  $t_2=8 \text{ s}$  for  $J_2$  (corresponding to  $\text{PS}_1$ ) and for the next 15 periods the etching times are  $t_1=20 \text{ s}$  for  $J_1$ , and  $t_2=8 \text{ s}$  for  $J_2$ . These last etching times correspond to  $\text{PS}_2$  and have been calculated from the etch rate to obtain the thicknesses adjusted during the simulation process of this PS.

The  $\text{PS}_2$  has been also fabricated to study its reflectivity spectrum and compare it with the one of the stacked structure. The parameters used for its fabrication are the same than for  $\text{PS}_1$ , therefore the refractive indices of the layers of this  $\text{PS}_2$  are expected to be the same than the ones of  $\text{PS}_1$ . The etching times are  $t_1=20 \text{ s}$  for  $J_1$ , and  $t_2=8 \text{ s}$  for  $J_2$ , the same ones used for the stacked structure.

The reflectivity spectrum of the stacked multilayer is presented in Fig. 7.16 for incidence angle  $\theta=12^\circ$ . It is compared with the measured reflectivity spectra of  $\text{PS}_1$  and  $\text{PS}_2$  for the same incidence angle. They have been measured with the FTIR spectrometer Bruker Vertex 70 at the wavelength range from 1 to  $3 \mu\text{m}$ . It can be observed that the bandgap of the stacked structure is wider than the bandgaps of  $\text{PS}_1$  and  $\text{PS}_2$  and is approximately the union of their bandgaps, as was expected. The bandgap of the stacked structure is slightly shifted to lower wavelengths than the bandgaps of  $\text{PS}_1$  and  $\text{PS}_2$ . This is due to two effects: the small gradients of porosity and thickness with depth during the porous silicon fabrication process that are more visible in the stacked structure spectrum because this structure is thicker than the PS; and that the thicknesses of the layers in multilayers are systematically lower than the expected values calculated from the etch rate [19]. Apart from this small shift, we can clearly observe the widening of the bandgap.

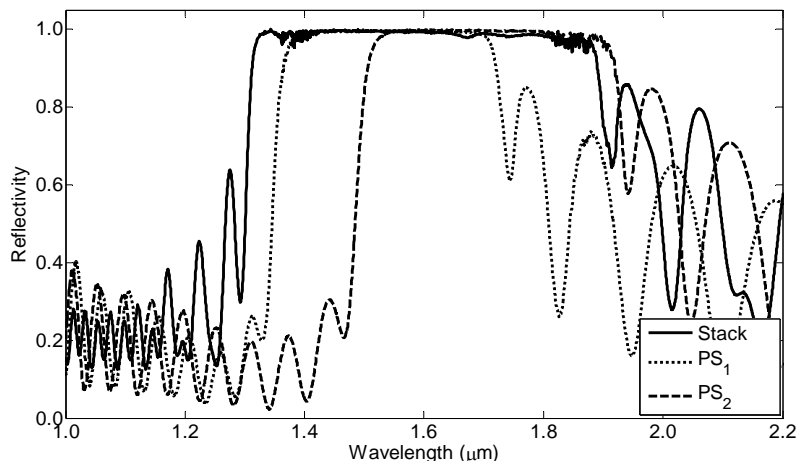


Fig. 7.16. Measured reflectivity spectrum of the stacked structure for  $\theta=12^\circ$  (solid line). The measured reflectivity spectra of  $PS_1$  and  $PS_2$  for the same incidence angle can be also observed (dashed lines).

The widening of the bandgap can be observed for the rest of incidence angles in Fig. 7.17. It can be supposed that if the bandgap for each incidence angle is wider, the multilayer could present an omnidirectional bandgap or at least a bandgap for a wider interval of incidence angles. In this figure we can observe that there exists a bandgap for the incidence angle range from  $12^\circ$  to  $60^\circ$ . For incidence angles  $70^\circ$  and  $80^\circ$  the bandgap is suggested but the measurement is falsified due to the influence of the sample holder of the FTIR.

Although the limits of our FTIR do not permit us to obtain good reflectivity spectrum measurements for  $\theta < 12^\circ$  and  $\theta > 65^\circ$ , the measurements for incidence angle  $70^\circ$  and  $80^\circ$  seem to indicate that the stacked structure has an omnidirectional bandgap. In order to verify that this structure is an omnidirectional mirror we have simulated it to check the existence of the bandgap for  $\theta < 12^\circ$  and  $\theta > 65^\circ$ .

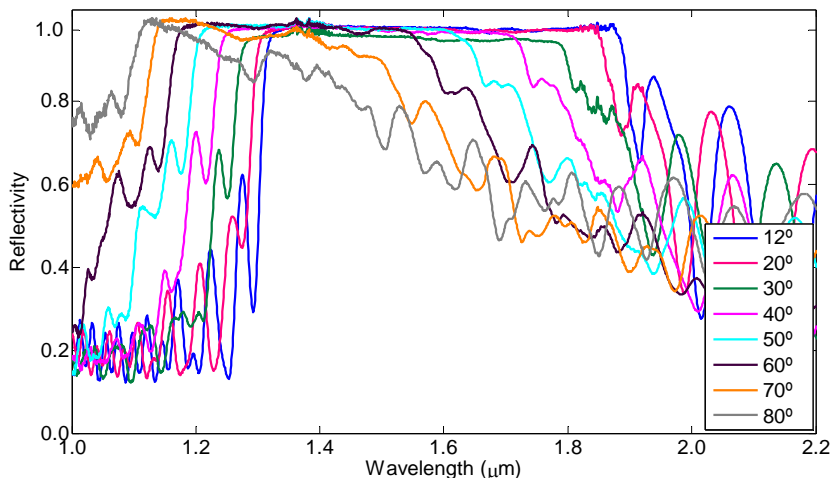


Fig. 7.17. Measured reflectivity spectrum of the stacked structure for different incidence angles.

A model of the stacked structure has been realized to simulate the bandgap for  $\theta < 12^\circ$  and  $\theta > 65^\circ$ . Fig. 7.18 shows the measured and the simulated reflectivity spectra of the stacked structure for incidence angle  $12^\circ$ . The parameters used for the model are for  $PS_1$ :  $n_1=2.1$ ,  $n_2=1.45$ ,  $d_1=168$  nm and  $d_2=265$  nm. And for  $PS_2$ :  $n_1=2.15$ ,  $n_2=1.45$ ,  $d_1=210$  nm and  $d_2=261$  nm. These refractive index values completely agree with the ones expected from the calibration of the system and the simulations of  $PS_1$  and  $PS_2$ . A small gradient of refractive index and thickness has been included in the simulation values. The thicknesses are slightly lower than the ones calculated from the etch rate according to what has been observed in the comparison between the PS multilayers and the stacked structure (Fig. 7.16) and according with the literature [19].

In Fig. 7.18, we can observe that there is a good agreement between simulated and measured spectra. The bandgap for both exists for the same wavelength range. The sidelobes also exist for the same wavelengths although there is a small difference between the simulated and the measured amplitudes due to the anisotropy of the low refractive index layers (see chapter 6) that is

not considered for the simulation program. The good agreement between simulation and measurement exists for all the incidence angles measured and in Fig. 7.18 we show the results for two of them. The simulation model is validated by the good agreement between the simulated and the measured reflectivity spectra.

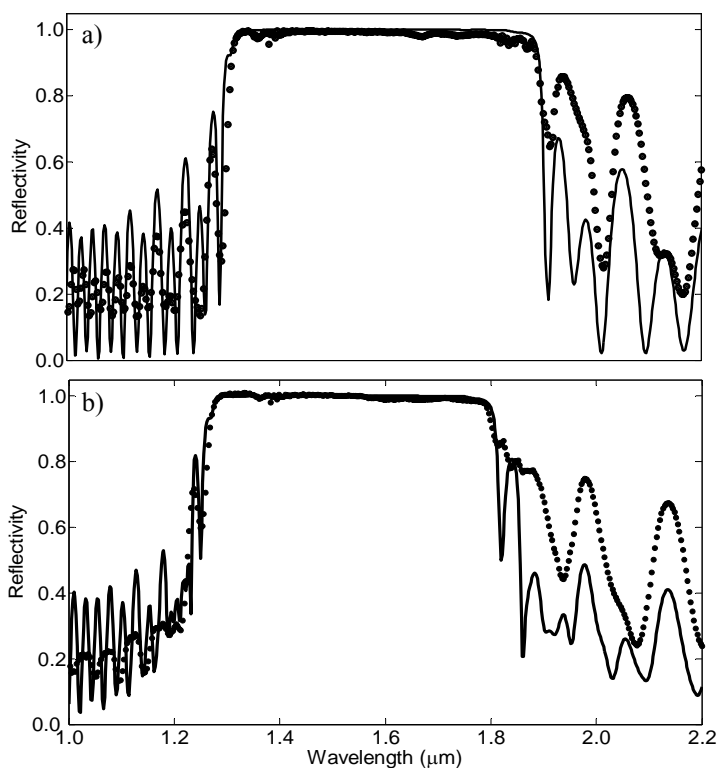


Fig. 7.18. Measured (symbols) and simulated (solid line) reflectivity spectra of the multilayer for incidence angle a) 12° and b) 30°.

With the simulation model we can study the existence of the omnidirectional bandgap suggested by the measurements. Fig. 7.19 shows the simulated reflectivity spectra for 0° and 85° obtained with this model. The

omnidirectional bandgap with a reflectivity higher than 95 % can be observed for the wavelength range between 1.32 and 1.44  $\mu\text{m}$ . This result supports the assumption that this stacked structure is an omnidirectional mirror.

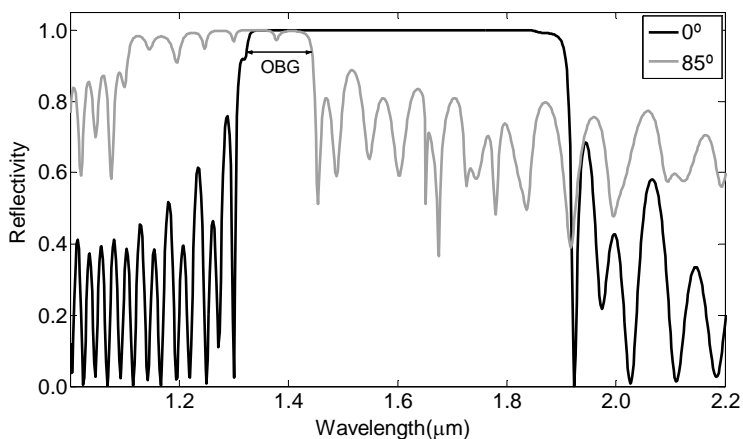


Fig. 7.19. Simulated reflectivity spectra of the stacked structure for incidence angles  $\theta=0^\circ$  and  $\theta=85^\circ$ . The omnidirectional bandgap (OBG) is indicated.

### 7.3.4. Enlargement of the omnidirectional mirror bandgap

We now study the reflectivity spectrum of a stacked structure consisting of three different PS stacked together. By increasing the number of PS of the stacked structure, the bandgap for each incidence angle will be wider and therefore the omnidirectional bandgap will enlarge.

The three PS that form this structure are the two ones presented before ( $\text{PS}_1$  and  $\text{PS}_2$ ) and a third one,  $\text{PS}_3$ . The schematic of this stacked structure can be observed in Fig. 7.20. The number of periods of the PS used for the formation of this stacked structure are 14 for the first, 13 for the second and 14 for the third, therefore it is a unbalanced structure, one of the mirror structures proposed in the theoretical study of omnidirectional mirrors (chapter 4).

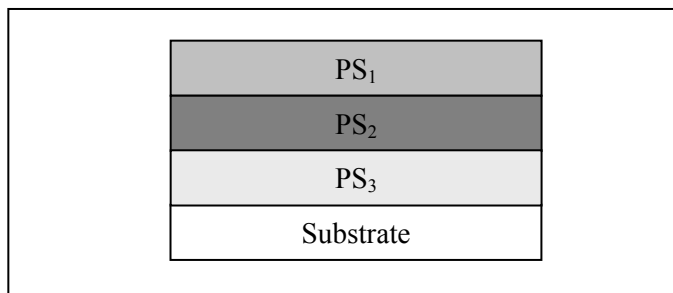


Fig. 7.20 Schematic of the stacked structure formed by three different periodic structures.

PS<sub>3</sub> consists of the periodic repetition of two layers obtained with current densities  $J_1=10 \text{ mA/cm}^2$  and  $J_2=50 \text{ mA/cm}^2$ , the same ones used for PS<sub>1</sub> and PS<sub>2</sub>. This PS<sub>3</sub> is designed to have a bandgap centered at a slightly higher wavelength than the one of PS<sub>2</sub>. For this reason, the thickness  $d_1$  (corresponding to  $J_1$ ) is slightly higher than the one of PS<sub>2</sub> for this layer whereas the thickness  $d_2$  remains the same. The period thickness is  $\Lambda = d_1 + d_2 = 545 \text{ nm}$ . The reflectivity spectrum of PS<sub>3</sub> has been simulated using  $n_1=2.15$  and  $n_2=1.45$ . Fig. 7.21 shows the simulated reflectivity spectrum of PS<sub>3</sub> for normal incidence and it is compared with the ones of PS<sub>1</sub> and PS<sub>2</sub>. The union of the three bandgaps is the expected bandgap of this stacked structure.

This stacked structure has been fabricated using  $p^+$ -type silicon wafers with a resistivity of  $0.01 \text{ } \Omega \cdot \text{cm}$  and ethanoic HF electrolyte with concentration of 15.4% (volumetric ratio). The current densities applied are  $J_1=10 \text{ mA/cm}^2$  and  $J_2=50 \text{ mA/cm}^2$ . For 14 periods the etching times are  $t_1=16 \text{ s}$  for  $J_1$ , and  $t_2= 8 \text{ s}$  for  $J_2$  (corresponding to PS<sub>1</sub>), for the next 13 periods the etching times are  $t_1= 20 \text{ s}$  for  $J_1$ , and  $t_2= 8 \text{ s}$  for  $J_2$  (corresponding to PS<sub>2</sub>), and the for last 14 periods the etching times are  $t_1=24 \text{ s}$  for  $J_1$ , and  $t_2= 8 \text{ s}$  for  $J_2$  (corresponding to PS<sub>3</sub>). These last etching times correspond to PS<sub>3</sub> and have been calculated from the etch rate to obtain the thicknesses calculated during the simulation process of this PS. The SEM image of this fabricated stacked structure can be observed in Fig. 7.22.



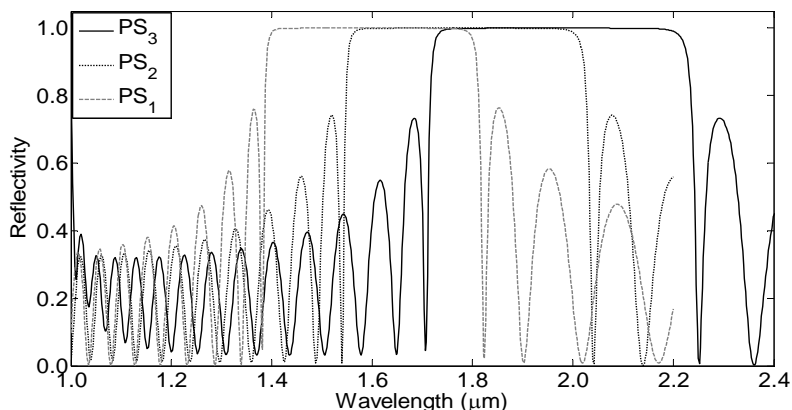


Fig. 7.21. Simulated reflectivity spectrum of  $PS_3$  for normal incidence (solid line) and simulated reflectivity spectra of  $PS_1$  and  $PS_2$  for the same incidence angle (dotted lines).

The reflectivity spectrum of the fabricated stacked structure has been measured with the FTIR spectrometer Bruker Vertex 70 for different incidence angles. These spectra can be observed in Fig. 7.23. For incidence angles between  $12^\circ$  and  $60^\circ$  the bandgap is clearly visible whereas for incidence angles  $70^\circ$  and  $76^\circ$  it can be supposed. From these results we can consider that this stacked structure is an omnidirectional mirror with a wider bandgap than the stacked structure presented in the previous section as was expected.

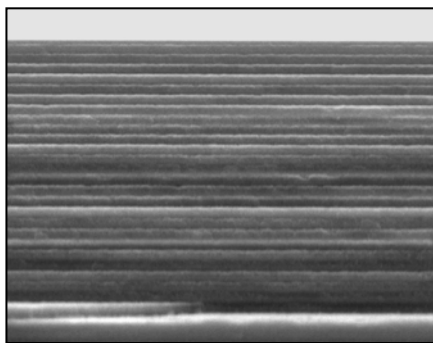


Fig. 7.22. SEM image of the fabricated stacked structure formed by three periodic structures.

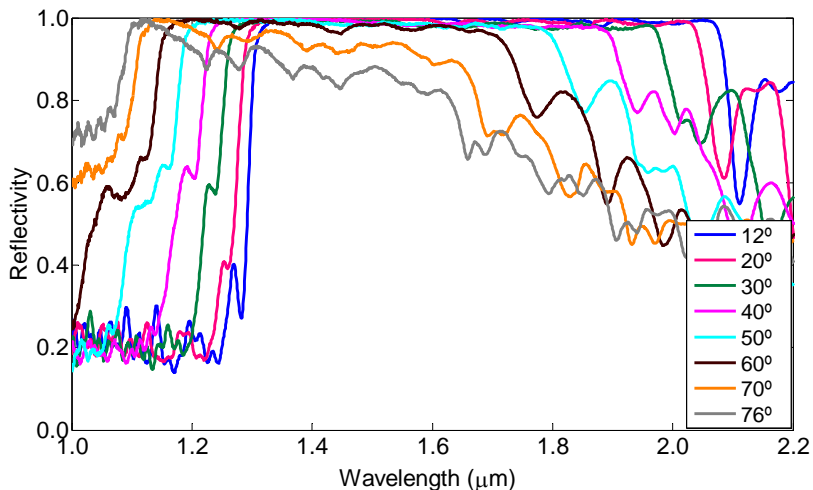


Fig. 7.23. Measured reflectivity spectra of the stacked structure for different incidence angles.

In order to study the reflectivity spectrum of the fabricated stacked structure for incidence angles  $\theta < 12^\circ$  and  $\theta > 65^\circ$  we have used a simulation model. The parameters used for the model are for PS<sub>1</sub>:  $n_1=2.1$ ,  $n_2=1.45$ ,  $d_1=160$  nm and  $d_2=270$  nm; for PS<sub>2</sub>:  $n_1=2.15$ ,  $n_2=1.45$ ,  $d_1=210$  nm and  $d_2=265$  nm and for PS<sub>3</sub>:  $n_1=2.2$ ,  $n_2=1.5$ ,  $d_1=240$  nm and  $d_2=265$  nm. These refractive index values completely agree with the ones expected from the previous studies and the simulations of PS<sub>1</sub> and PS<sub>2</sub>. We have simulated the refractive index gradient with depth by slightly increasing the refractive index of the PS. The thicknesses are slightly thinner than the ones expected from the etch rate calculation [19]. Fig. 7.24 shows the simulated reflectivity spectrum for two incidence angles. We can observe that the simulated reflectivity spectrum agrees with measured one, validating the model.

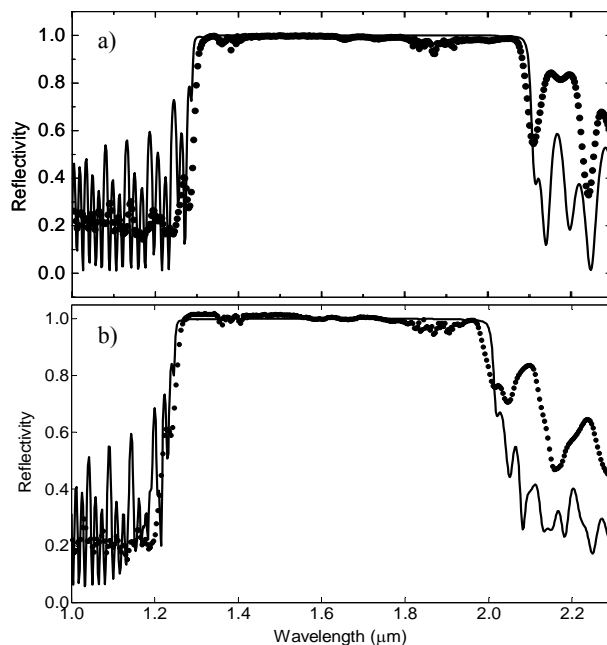


Fig. 7.24. Measured (symbols) and simulated (solid line) reflectivity spectra of the stacked structure for incidence angles a) 12° and b) 30°.

To study the omnidirectional bandgap (OBG) of this multilayer, we have used the model to simulate the reflectivity spectra for 0° and 85° (Fig. 7.25). In this figure, the OBG for reflectivity higher than 90 % exists for the wavelength range from 1.3 μm to 1.6 μm. Hence, we can conclude that this multilayer is an omnidirectional mirror. Besides, the omnidirectional bandgap of this multilayer is wider than the one of the multilayer studied in the previous section, consisting of two PS stacked together.

We can conclude that the stack of different PS is an appropriate structure to obtain porous silicon omnidirectional mirrors that cannot be obtained by increasing the refractive index contrast of the layers due to material limitations. The width of the omnidirectional bandgap can be selected by choosing the appropriate number of PS to be stacked and the wavelengths where they are centered.

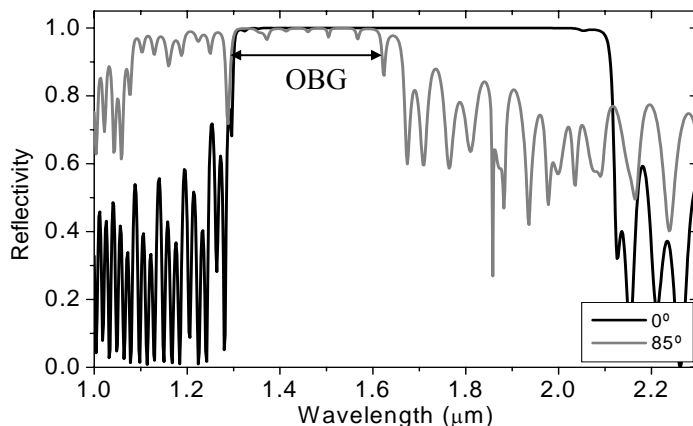


Fig. 7.25. Simulated reflectivity spectrum of the multilayer for incidence angles  $\theta=0^\circ$  and  $\theta=85^\circ$ . The omnidirectional bandgap (OBG) is indicated.

## 7.4. Conclusions

Many different porous silicon DBR, microcavities and omnidirectional mirrors have been designed, fabricated and characterized. In this chapter we have reported only the most representative.

The first optical device reported here is a porous silicon DBR. The reflectivity spectrum of this DBR has been measured for different angles of incidence. A high reflectivity band has been observed, that shifts to lower wavelengths, becomes narrower and its maximum decreases when the angle of incidence increases. The simulated spectra agree with the measured ones, which indicates that the behavior of the structure can be theoretically predicted. The refractive indices and thicknesses of the fabricated layers agree with the ones obtained with the simulations. It has also been demonstrated that for any wavelength, the range of incidence angles for which the bandgap exists can be studied with the projected band structure.

Porous silicon microcavities have also been fabricated, characterized and simulated. The reflectivity spectrum of the microcavity reported here has been measured for different humidity levels. We have observed that the reflectivity

spectrum not only depends on the humidity level of the ambient medium but also on the presence of a water thin film on its surface due to the condensation of water. In both cases, the reflectivity resonance shifts to higher wavelengths and the reflectivity decreases when the humidity increases, but the relative changes in the reflectivity spectrum are much more significant with the presence of condensed water.

Omnidirectional mirrors have also been designed, fabricated and characterized. Firstly, a periodic structure has been fabricated. It was formed by the periodic repetition of two different refractive index layer. The two refractive indices used are the lowest one and the highest one obtainable with our fabrication parameters. The reflectivity spectrum of this structure was measured and it indicated that with these refractive indices an omnidirectional bandgap can not be obtained. Secondly, a new structure consisting of different periodic structures stacked together has been used to obtain omnidirectional mirrors. The refractive indices used for this new structure have been the same used for the periodic structure. A first stacked structure consisting of two PS stacked together has been designed, fabricated and characterized demonstrating that it is possible to obtain omnidirectional mirrors without changing the refractive indices. The enlargement of the omnidirectional bandgap has been obtained with a second stacked structure consisting of three periodic structures stacked together. This is an unbalanced structure theoretically studied in chapter 4. With these results we have demonstrated that the refractive indices of the layers that form the multilayer are not a limitation for obtaining omnidirectional mirrors, as was for the periodic structure. We have also demonstrated that the new structure proposed in this work, formed by different periodic structures stacked together, is a suitable structure for obtaining wide band omnidirectional mirrors.

To conclude, it has been demonstrated that porous silicon is a suitable material for the fabrication of optical devices and that the material characteristics allows the application of these optical devices for the widely used in telecommunications wavelength of 1.55  $\mu\text{m}$ .